A phase-field model and its efficient numerical method for two-phase flows on arbitrarily curved surfaces in 3D space

Junxiang Yang, Junseok Kim*

Department of Mathematics, Korea University, Seoul, 02841, Republic of Korea

Abstract

Herein, we present a phase-field model and its efficient numerical method for incompressible single and binary fluid flows on arbitrarily curved surfaces in a three-dimensional (3D) space. An incompressible single fluid flow is governed by the Navier–Stokes (NS) equation and the binary fluid flow is governed by the two-phase Navier–Stokes–Cahn–Hilliard (NSCH) system. In the proposed method, we use a narrow band domain to embed the arbitrarily curved surface and extend the NSCH system and apply a pseudo-Neumann boundary condition that enforces constancy of the dependent variables along the normal direction of the points on the surface. Therefore, we can use the standard discrete Laplace operator instead of the discrete Laplace–Beltrami operator. Within the narrow band domain, the Chorin's projection method is applied to solve the NS equation, and a convex splitting method is employed to solve the Cahn–Hilliard equation with an advection term. To keep the velocity field tangential to the surface, a velocity correction procedure is applied. An effective mass correction step is adopted to preserve the phase concentration. Computational results such as convergence test, Kevin–Helmholtz instability, and Rayleigh–Taylor instability on curved surfaces demonstrate the accuracy and efficiency of the proposed method.
© 2020 Elsevier B.V. All rights reserved.

Keywords: Two-phase fluid flow; Cahn–Hilliard equation; Kevin–Helmholtz instability; Rayleigh–Taylor instability

1. Introduction

The Navier–Stokes (NS) equation is a well-known mathematical model used to describe the dynamics of incompressible fluid flows. However, the existence of the nonlinear advection term typically results in difficulties in the analytical study of the NS equation. Therefore, the NS equation must be solved using numerical methods. To overcome the difficulty arising from a coupling of the pressure and velocity, a projection method [1,2] was developed. Based on the classical projection method, Shen [3] proposed a pressure correction approach to improve the accuracy of the pressure on the boundary. To efficiently solve problems with a large density ratio, a pressure stabilized method [4] was developed. In addition, various computational approaches for solving the NS equation have been proposed [5–12].

Compared with a single fluid flow, a binary (two-phase) fluid flow is more important because several physical problems contain more than one component. During the past 20 years, the phase-field method has become

an effective technique for modeling multi-phase problems because a topological change in the interface can be implicitly captured by solving the equation. The most well-known phase-field model for multi-phase flow problems is the Navier–Stokes–Cahn–Hilliard (NSCH) equation. Previous publications have reported the applications of the NSCH equations in multi-component fluid flows [13–24]. Although many computational methods work well for the NSCH equations in two- and three-dimensional spaces, most of them are limited to rectangular or cuboid domains.

The evolution of a dynamic system on an arbitrarily curved 3D surface is an important problem. Various practical numerical schemes have been developed for solving the partial differential equations with scalar variables, such as the Cahn–Hilliard (CH) [25–29], Allen–Cahn (AC) [30,31], phase-field crystal (PFC) [32,33], and Ohta–Kawasaki (OK) equations [34]. However, there have been few numerical simulations of fluid flows on arbitrarily curved 3D surfaces. At present, the discrete exterior calculus (DEC) method and surface finite element method are two effective methods for solving the NS equation on a curved surface. A conservative scheme for the incompressible NS equation on surfaces was proposed by Mohamed et al. [35]. The proposed scheme has a second- and first-order accuracy for structured and unstructured meshes, respectively. Nitschke et al. [36] applied the DEC method to solve the fluid equation with a vorticity-stream function on curved surfaces. Using the surface finite element, Reuther and Voigt [37] solved the incompressible NS equation on curved surfaces. Recently, Yang et al. [38] developed a practical numerical scheme for simulating the NS equation on a curved surface. In their study, the velocity field and pressure are both defined at the cell corners. Ambrus et al. [39] used the lattice Boltzmann method to investigate the two-phase hydrodynamic phase separation on a torus. Nitschke et al. [40] investigated the phase separation and buoyancy-driven flow on a sphere and torus by applying the finite element approach. In the present study, a staggered marker-and-cell (MAC) [41] mesh is applied, i.e., the velocities are stored at the cell edges, and the pressure and phase variable are stored at the cell centers. To the best of our knowledge, this is the first study focusing on single and two-phase incompressible fluid flows on a curved 3D surface by using the finite difference method and MAC mesh.

We use a projection method [1] to solve the incompressible NS equation. Using a velocity correction step, we keep the velocity field tangential to the surface. The convex splitting method [42] is used to solve the CH equation and an effective mass correction algorithm is adopted to preserve the mass conservation. The proposed scheme is simple to implement because the standard seven-point finite difference Laplace operator is used.

The remainder of this paper is organized as follows. In Section 2, we describe the incompressible NSCH model in a narrow band domain in a 3D space. In Section 3, we provide the numerical solutions for the NS equation and the convective CH equation. Various numerical experiments are presented in Section 4. Finally, some concluding remarks are provided in Section 5.

2. Incompressible NSCH system on a narrow band domain

We briefly review the following dimensionless incompressible NSCH system on a curved surface S in a 3D space $\mathbb{R}^3$. For $\mathbf{x} \in S,\ t > 0$,

$$\rho(\phi(\mathbf{x}, t))\left(\frac{\partial \mathbf{u}(\mathbf{x}, t)}{\partial t} + \mathbf{u}(\mathbf{x}, t) \cdot \nabla_s \mathbf{u}(\mathbf{x}, t)\right) = -\nabla_s p(\mathbf{x}, t) + \frac{1}{BoCn}\mu(\mathbf{x}, t)\nabla_s \phi(\mathbf{x}, t)$$

$$+ \frac{1}{Re}\nabla_s \cdot \left[\eta(\phi(\mathbf{x}, t))(\nabla_s \mathbf{u}(\mathbf{x}, t) + \nabla_s \mathbf{u}(\mathbf{x}, t)^T)\right] + \frac{\rho(\phi(\mathbf{x}, t))}{Fr^2}\mathbf{g}, \tag{1}$$

$$\nabla_s \cdot \mathbf{u}(\mathbf{x}, t) = 0, \tag{2}$$

$$\frac{\partial \phi(\mathbf{x}, t)}{\partial t} + \nabla_s \cdot [\phi(\mathbf{x}, t)\mathbf{u}(\mathbf{x}, t)] = \frac{1}{Pe}\Delta_s \mu(\mathbf{x}, t), \tag{3}$$

$$\mu(\mathbf{x}, t) = F'(\phi(\mathbf{x}, t)) - Cn^2 \Delta_s \phi(\mathbf{x}, t). \tag{4}$$

Note that $p(\mathbf{x}, t) = \hat{p}(\mathbf{x}, t) + \frac{1}{BoCn}\phi(\mathbf{x}, t)\mu(\mathbf{x}, t)$ is a modified pressure field and $\hat{p}(\mathbf{x}, t)$ is the original pressure field. In addition, $\mathbf{u}(\mathbf{x}, t) = (u(\mathbf{x}, t), v(\mathbf{x}, t), w(\mathbf{x}, t))$, $\phi(\mathbf{x}, t)$, and $\mu(\mathbf{x}, t)$ are the velocity field, phase variable, and chemical potential, respectively. In addition, $F(\phi(\mathbf{x}, t)) = F(\phi) = 0.25(\phi^2 - 1)^2$ is the fourth-order polynomial potential functional and $F'(\phi(\mathbf{x}, t)) = F'(\phi) = \phi^3 - \phi$ is the derivative of $F(\phi)$ with respect to ϕ. Note that $\nabla_s = \mathbf{P}\nabla$ and $\Delta_s = \nabla \cdot (\mathbf{P}\nabla)$ indicate the surface gradient operator and surface Laplace–Beltrami operator, respectively, where $\mathbf{P} = \mathbf{I} - (\nabla d)^T \nabla d$ [32,43,44]. Here, $d : \mathbb{R}^3 \to \mathbb{R}$ is a signed distance function and $S = \{\mathbf{x} \in \mathbb{R}^3|\ d(\mathbf{x}) = 0\}$. Let $\Omega_\delta = \{\mathbf{y}|\ \mathbf{y} = \mathbf{x} + \theta\mathbf{n}(\mathbf{x})\ \text{for}\ |\theta| < \delta,\ \mathbf{x} \in S\}$ be the δ-neighborhood narrow band of S, where $\mathbf{n}(\mathbf{x})$ is a unit normal
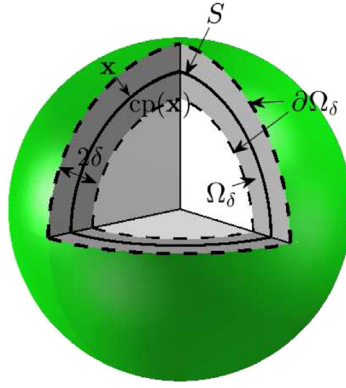
Fig. 1. Schematic illustration of Ω_δ, $\partial\Omega_\delta$, S, and cp($\mathbf{x}$).

vector at $\mathbf{x}$. The dimensionless parameters used are as follows: the Reynolds number $Re = \rho_c L_c U_c / \eta_c$, the Cahn number $Cn = \epsilon/L_c$, the Bone number $Bo = We/Fr^2$, where $We = \rho_c U_c^2 L_c/\sigma$ is the Weber number, Froude number $Fr = U_c/\sqrt{gL_c}$, and Peclet number $Pe = U_c L_c/(M\mu_c)$. Here, ρ_c and η_c are the characteristic density and viscosity, respectively. In addition, L_c, U_c, σ, g, M, and μ_c are the characteristic length, characteristic velocity, surface tension coefficient, gravitational acceleration, mobility, and characteristic chemical, respectively, and ϵ is a small positive parameter related to the width of a diffusive interface. The density and viscosity of the whole system is defined as $\rho(\phi(\mathbf{x}, t)) = \rho_1(1 + \phi(\mathbf{x}, t))/2 + \rho_2(1 - \phi(\mathbf{x}, t))/2$, $\eta(\phi(\mathbf{x}, t)) = \eta_1(1 + \phi(\mathbf{x}, t))/2 + \eta_2(1 - \phi(\mathbf{x}, t))/2$, where ρ_1 and ρ_2 are the densities of fluid 1 and fluid 2, and η_1 and η_2 are the viscosities of fluid 1 and fluid 2, respectively. More details on various dimensionless parameters are provided in [45]. If δ is small, then p, ϕ, and μ have constant values in the direction normal to S. Thus, $\mathbf{P} = \mathbf{I}$ is approximately satisfied, and the Laplace–Beltrami operator can be replaced by the standard Laplace operator [46]. Next, we extend Eqs. (1)–(4) to the narrow band domain Ω_δ:

$$\rho(\phi(\mathbf{x}, t))\left(\frac{\partial \mathbf{u}(\mathbf{x}, t)}{\partial t} + \mathbf{u}(\mathbf{x}, t) \cdot \nabla\mathbf{u}(\mathbf{x}, t)\right) = -\nabla p(\mathbf{x}, t) + \frac{1}{BoCn}\mu(\mathbf{x}, t)\nabla\phi(\mathbf{x}, t)$$

$$+ \frac{1}{Re}\nabla \cdot \left[\eta(\phi(\mathbf{x}, t))(\nabla\mathbf{u}(\mathbf{x}, t) + \nabla\mathbf{u}(\mathbf{x}, t)^t)\right] + \frac{\rho(\phi(\mathbf{x}, t))}{Fr^2}\mathbf{g}, \tag{5}$$

$$\nabla \cdot \mathbf{u}(\mathbf{x}, t) = 0, \tag{6}$$

$$\frac{\partial \phi(\mathbf{x}, t)}{\partial t} + \nabla \cdot [\phi(\mathbf{x}, t)\mathbf{u}(\mathbf{x}, t)] = \frac{1}{Pe}\Delta\mu(\mathbf{x}, t), \tag{7}$$

$$\mu(\mathbf{x}, t) = F'(\phi(\mathbf{x}, t)) - Cn^2\Delta\phi(\mathbf{x}, t), \tag{8}$$

where $\mathbf{x} \in \Omega_\delta$ and $t > 0$. We use pseudo-Neumann boundary conditions for p, ϕ, and μ:

$$p(\mathbf{x}, t) = p(\text{cp}(\mathbf{x}), t), \ \ \phi(\mathbf{x}, t) = \phi(\text{cp}(\mathbf{x}), t), \ \ \mu(\mathbf{x}, t) = \mu(\text{cp}(\mathbf{x}), t) \text{ on } \partial\Omega_\delta, \tag{9}$$

where cp($\mathbf{x}$) $\in S$ for $\mathbf{x} \in \partial\Omega_\delta$ [47] (see Fig. 1). A detailed discussion of the boundary conditions of the velocity field is provided in Section 3.

3. Numerical solutions

In this section, we present the numerical solutions for the NSCH system. The NSCH system is discretized in $\Omega = (a, b) \times (c, d) \times (e, f)$ embedding $\Omega_\delta \cup U_\delta \cup V_\delta \cup W_\delta$. Let N_x, N_y, and N_z be positive integers, $h = (b-a)/N_x = (d-c)/N_y = (f-e)/N_z$ be the space step, and $\Omega^h = \{\mathbf{x}_{ijk} = (x_i, y_j, z_k) = (a + (i - 0.5)h, c + (j - 0.5)h, e + (k - 0.5)h)| \ 1 \le i \le N_x, 1 \le j \le N_y, 1 \le k \le N_z\}$ be the set of cell centers. The sets of cell edges are defined as
$U^h = \{\mathbf{x}_{i+\frac{1}{2},jk} = (x_{i+\frac{1}{2}}, y_j, z_k) = (a + ih, c + (j - 0.5)h, e + (k - 0.5)h)| \ 0 \le i \le N_x, 1 \le j \le N_y, 1 \le k \le N_z\}$,
$V^h = \{\mathbf{x}_{i,j+\frac{1}{2},k} = (x_i, y_{j+\frac{1}{2}}, z_k) = (a + (i - 0.5)h, c + jh, e + (k - 0.5)h)| \ 1 \le i \le N_x, 0 \le j \le N_y, 1 \le k \le N_z\}$,
$W^h = \{\mathbf{x}_{ij,k+\frac{1}{2}} = (x_i, y_j, z_{k+\frac{1}{2}}) = (a + (i - 0.5)h, c + (j - 0.5)h, e + kh)| \ 1 \le i \le N_x, 1 \le j \le N_y, 0 \le k \le N_z\}$.

In this study, the discrete pressure p, phase variable ϕ, and chemical potential μ are stored at the cell centers, and the discrete velocities u, v, and w are stored at the cell edges. Let $u^n_{i+\frac{1}{2},jk}$, $v^n_{i,j+\frac{1}{2},k}$, $w^n_{ij,k+\frac{1}{2}}$, p^n_{ijk}, ϕ^n_{ijk}, and μ^n_{ijk} be discrete approximations of $u(\mathbf{x}_{i+\frac{1}{2},jk}, n\Delta t)$, $v(\mathbf{x}_{i,j+\frac{1}{2},k}, n\Delta t)$, $w(\mathbf{x}_{ij,k+\frac{1}{2}}, n\Delta t)$, $p(\mathbf{x}_{ijk}, n\Delta t)$, $\phi(\mathbf{x}_{ijk}, n\Delta t)$, and $\mu(\mathbf{x}_{ijk}, n\Delta t)$, respectively, where Δt is the time step. Let $d : \mathbb{R}^3 \to \mathbb{R}$ be the signed distance function and $S = \{\mathbf{x} \in \mathbb{R}^3 | \ d(\mathbf{x}) = 0\}$. Let $\Omega^h_\delta = \{\mathbf{x}_{ijk}| \ |d_{ijk}| < \delta|\nabla_h d_{ijk}|\}$ be the discrete narrow band domain, where $\nabla_h d_{ijk} = (d_{i+1,jk}-d_{i-1,jk}, d_{i,j+1,k}-d_{i,j-1,k}, d_{ij,k+1}-d_{ij,k-1})/(2h)$ and $\delta > \sqrt{3}h$. The discrete narrow band domains containing values at cell edges are defined as $U^h_\delta = \{\mathbf{x}_{i+\frac{1}{2},jk}, \ \mathbf{x}_{i-\frac{1}{2},jk}| \ \mathbf{x}_{ijk} \in \Omega^h_\delta\}$, $V^h_\delta = \{\mathbf{x}_{i,j+\frac{1}{2},k}, \ \mathbf{x}_{i,j-\frac{1}{2},k}| \ \mathbf{x}_{ijk} \in \Omega^h_\delta\}$, $W^h_\delta = \{\mathbf{x}_{ij,k+\frac{1}{2}}, \ \mathbf{x}_{ij,k-\frac{1}{2}}| \ \mathbf{x}_{ijk} \in \Omega^h_\delta\}$, respectively. Let $\partial\Omega^h_\delta = \{\mathbf{x}_{ijk}| \ I_{ijk}|\nabla_h I_{ijk}| \neq 0\}$ be the discrete boundary for the cell centers. Here, $I_{ijk} = 0$ if $\mathbf{x}_{ijk} \in \Omega^h_\delta$; otherwise $I_{ijk} = 1$. The discrete boundary for the cell edges ∂U^h_δ, ∂V^h_δ, and ∂W^h_δ can be easily defined in the same way. We first define the temporal discretization of the NSCH system as follows:

$$\rho^n \frac{\mathbf{u}^{n+1} - \mathbf{u}^n}{\Delta t} = -\rho^n \mathbf{u}^n \cdot \nabla \mathbf{u}^n - \nabla p^{n+1} + \frac{1}{BoCn}\mu^n \nabla \phi^n$$

$$+ \frac{1}{Re}\nabla \cdot \left[\eta^n(\nabla\mathbf{u} + \nabla\mathbf{u}^T)^n\right] + \frac{\rho^n}{Fr^2}\mathbf{g}, \tag{10}$$

$$\nabla \cdot \mathbf{u}^{n+1} = 0, \tag{11}$$

$$\frac{\phi^{n+1} - \phi^n}{\Delta t} = -\nabla \cdot (\phi\mathbf{u})^n + \frac{1}{Pe}\Delta\mu^{n+1}, \tag{12}$$

$$\mu^{n+1} = (\phi^{n+1})^3 - \phi^n - Cn^2\Delta\phi^{n+1}, \tag{13}$$

where $\rho^n = \rho(\phi^n)$, $\eta^n = \eta(\phi^n)$, and $\mathbf{g} = (0, 0, -1)$. Here, the temporally first-order accurate, semi-implicit scheme is used for Eqs. (10)–(13). The surface tension, gravity, and velocity components on the right-hand side of Eq. (10) are treated explicitly, and the pressure gradient is treated implicitly. In Eqs. (12) and (13), all Laplacian parts are treated implicitly, and the convection term is treated explicitly. Following the idea of a convex splitting method, in Eq. (13), we treat the nonlinear convex and concave parts implicitly and explicitly.

3.1. Navier–Stokes solver

In this section, we solve the NS equation in the fully discrete space $U^h_\delta \cup V^h_\delta \cup W^h_\delta$ using the following steps:

Step 1. Define the divergence-free initial discrete velocities $u^0_{i+\frac{1}{2},jk}$, $v^0_{i,j+\frac{1}{2},k}$, $w^0_{ij,k+\frac{1}{2}}$, and the initial discrete phase variable ϕ^0_{ijk}.

Step 2. The intermediate velocities $u^*_{i+\frac{1}{2},jk}$, $v^*_{i,j+\frac{1}{2},k}$, and $w^*_{ij,k+\frac{1}{2}}$ are calculated as follows:

$$u^*_{i+\frac{1}{2},jk} = u^n_{i+\frac{1}{2},jk} - \Delta t(\mathbf{u}^n \cdot \nabla_h u^n)_{i+\frac{1}{2},jk} + \frac{\Delta t}{Re\rho_{i+\frac{1}{2},jk}}Du(\mathbf{u}^n)_{i+\frac{1}{2},jk}$$

$$+ \frac{\Delta t \mu^n_{i+\frac{1}{2},jk}}{BoCn\rho^n_{i+\frac{1}{2},jk}}\left(\frac{\phi^n_{i+1,jk} - \phi^n_{ijk}}{h}\right) \tag{14}$$

$$v^*_{i,j+\frac{1}{2},k} = v^n_{i,j+\frac{1}{2},k} - \Delta t(\mathbf{u}^n \cdot \nabla_h v^n)_{i,j+\frac{1}{2},k} + \frac{\Delta t}{Re\rho_{i,j+\frac{1}{2},k}}Dv(\mathbf{u}^n)_{i,j+\frac{1}{2},k}$$

$$+ +\frac{\Delta t\mu^n_{i,j+\frac{1}{2},k}}{BoCn\rho^n_{i,j+\frac{1}{2},k}}\left(\frac{\phi^n_{i,j+1,k} - \phi^n_{ijk}}{h}\right) \tag{15}$$

$$w^*_{ij,k+\frac{1}{2}} = w^n_{ij,k+\frac{1}{2}} - \Delta t(\mathbf{u}^n \cdot \nabla_h w^n)_{ij,k+\frac{1}{2}}\frac{\Delta t}{Re\rho_{ij,k+\frac{1}{2}}}Dw(\mathbf{u}^n)_{ij,k+\frac{1}{2}}$$

$$+ \frac{\Delta t\mu^n_{ij,k+\frac{1}{2}}}{BoCn\rho^n_{ij,k+\frac{1}{2}}}\left(\frac{\phi^n_{ij,k+1} - \phi^n_{ijk}}{h}\right) - \frac{\Delta t}{Fr^2}g, \tag{16}$$

where $\rho^n_{i+\frac{1}{2},jk} = 0.5(\rho^n_{i+1,jk}+\rho^n_{ijk})$, $\rho^n_{i,j+\frac{1}{2},k} = 0.5(\rho^n_{i,j+1,k}+\rho^n_{ijk})$, and $\rho^n_{ij,k+\frac{1}{2}} = 0.5(\rho^n_{ij,k+1}+\rho^n_{ijk})$. For the advection term, the first-order upwind scheme is simple and stable [48,49]. To achieve a second-order spatial accuracy, the central difference has been widely used in some previous studies [50,51]. However, the classical central difference scheme suffers from a stability problem. In our approach, we use a second-order essentially non-oscillatory (ENO) scheme [52,53] to discretize the advection terms in Eqs. (14)–(16). For example, the advection term in Eq. (14) is discretized as follows:

$$
\begin{aligned}
(\mathbf{u} \cdot \nabla_h u)_{i+\frac{1}{2},jk} &= \frac{u_{i+\frac{1}{2},jk}}{h} \left(\bar{u}_{i+1,jk} - \bar{u}_{ijk} \right) \\
&+ \frac{v_{i,j-\frac{1}{2},k} + v_{i+1,j-\frac{1}{2},k} + v_{i,j+\frac{1}{2},k} + v_{i+1,j+\frac{1}{2},k}}{4h} \left(\bar{u}_{i+\frac{1}{2},j+\frac{1}{2},k} - \bar{u}_{i+\frac{1}{2},j-\frac{1}{2},k} \right) \\
&+ \frac{w_{ij,k-\frac{1}{2}} + w_{i+1,j,k-\frac{1}{2}} + w_{ij,k+\frac{1}{2}} + w_{i+1,j,k+\frac{1}{2}}}{4h} \left(\bar{u}_{i+\frac{1}{2},j,k+\frac{1}{2}} - \bar{u}_{i+\frac{1}{2},j,k-\frac{1}{2}} \right).
\end{aligned}
$$

The algorithm for calculating $\bar{u}_{i+1,jk}$ is given as

$$
\bar{u}_{i+1,jk} = u_{ljk} + \frac{h}{2}\gamma(1 - 2(l - (i + \frac{1}{2}))),
$$

$$
l = \begin{cases} i + \frac{1}{2} & \text{if } u_{i+1,jk} > 0, \\ i + \frac{3}{2} & \text{otherwise,} \end{cases}
$$

$$
\alpha = \frac{u_{ljk} - u_{l-1,jk}}{h}, \quad \beta = \frac{u_{l+1,jk} - u_{ljk}}{h}, \quad \gamma = \begin{cases} \alpha & \text{if } |\alpha| \leq |\beta|, \\ \beta & \text{otherwise,} \end{cases}
$$

where $u_{i+1,jk} = 0.5\left(u_{i+\frac{3}{2},jk} + u_{i+\frac{1}{2},jk}\right)$. The other quantities are calculated in a similar manner. The discrete advection terms for v and w are presented in Appendix. The spatial discretization for the viscosity term in Eq. (14) is defined as

$$
\begin{aligned}
Du(\mathbf{u})_{i+\frac{1}{2},jk} &= \frac{2\left(\eta(\phi_{i+1,jk})(u_{i+\frac{3}{2},jk} - u_{i+\frac{1}{2},jk}) - \eta(\phi_{ijk})(u_{i+\frac{1}{2},jk} - u_{i-\frac{1}{2},jk})\right)}{h^2} \\
&+ \frac{\eta_a(u_{i+\frac{1}{2},j+1,k} - u_{i+\frac{1}{2},jk}) - \eta_b(u_{i+\frac{1}{2},jk} - u_{i+\frac{1}{2},j-1,k})}{h^2} \\
&+ \frac{\eta_a(v_{i+1,j+\frac{1}{2},k} - v_{i,j+\frac{1}{2},k}) - \eta_b(v_{i+1,j-\frac{1}{2},k} - v_{i,j-\frac{1}{2},k})}{h^2} \\
&+ \frac{\eta_c(u_{i+\frac{1}{2},j,k+1} - u_{i+\frac{1}{2},jk}) - \eta_d(u_{i+\frac{1}{2},jk} - u_{i+\frac{1}{2},j,k-1})}{h^2} \\
&+ \frac{\eta_c(w_{i+1,j,k+\frac{1}{2}} - w_{ij,k+\frac{1}{2}}) - \eta_d(w_{i+1,j,k-\frac{1}{2}} - w_{ij,k-\frac{1}{2}})}{h^2},
\end{aligned}
$$

where the η_a, η_b, η_c, and η_d are defined as follows:

$$
\begin{aligned}
\eta_a &= 0.25\left(\eta(\phi_{ijk}) + \eta(\phi_{i+1,jk}) + \eta(\phi_{i,j+1,k}) + \eta(\phi_{i+1,j+1,k})\right), \\
\eta_b &= 0.25\left(\eta(\phi_{ijk}) + \eta(\phi_{i+1,jk}) + \eta(\phi_{i,j-1,k}) + \eta(\phi_{i+1,j-1,k})\right), \\
\eta_c &= 0.25\left(\eta(\phi_{ijk}) + \eta(\phi_{i+1,jk}) + \eta(\phi_{i+1,j,k+1}) + \eta(\phi_{ij,k+1})\right), \\
\eta_d &= 0.25\left(\eta(\phi_{ijk}) + \eta(\phi_{i+1,jK}) + \eta(\phi_{i+1,j,k-1}) + \eta(\phi_{ij,k-1})\right).
\end{aligned}
$$

The similar definitions are used for computing $Dv(\mathbf{u})_{i,j+\frac{1}{2},k}$ and $Dw(\mathbf{u})_{ijk+\frac{1}{2}}$.

Step 3. We solve Eqs. (17) and (18)

$$
\frac{\mathbf{u}^{n+1,1} - \mathbf{u}^*}{\Delta t} = -\frac{1}{\rho^n}\nabla_h p^{n+1}, \tag{17}
$$

$$
\nabla_h \cdot \mathbf{u}^{n+1,1}_{ijk} = 0. \tag{18}
$$

Taking the discrete divergence operation to Eq. (17) and using Eq. (18), we obtain the following:

$$\nabla_h \cdot \left(\frac{1}{\rho^n} \nabla_h p^{n+1} \right) = \frac{1}{\Delta t} \nabla_h \cdot \mathbf{u}^*, \tag{19}$$

where

$$
\nabla_h \cdot \left(\frac{1}{\rho^n} \nabla_h p_{ijk}^{n+1} \right)
$$
$$
= \left[\frac{p_{i+1,jk}^{n+1}}{\rho_{i+\frac{1}{2},jk}^n} + \frac{p_{i-1,jk}^{n+1}}{\rho_{i-\frac{1}{2},jk}^n} + \frac{p_{i,j+1,k}^{n+1}}{\rho_{i,j+\frac{1}{2},k}^n} + \frac{p_{i,j-1,k}^{n+1}}{\rho_{i,j-\frac{1}{2},k}^n} + \frac{p_{ij,k+1}^{n+1}}{\rho_{ij,k+\frac{1}{2}}^n} + \frac{p_{ij,k-1}^{n+1}}{\rho_{ij,k-\frac{1}{2}}^n} \right.
$$
$$
\left. - \left(\frac{1}{\rho_{i+\frac{1}{2},jk}^n} + \frac{1}{\rho_{i-\frac{1}{2},jk}^n} + \frac{1}{\rho_{i,j+\frac{1}{2},k}^n} + \frac{1}{\rho_{i,j-\frac{1}{2},k}^n} + \frac{1}{\rho_{ij,k+\frac{1}{2}}^n} + \frac{1}{\rho_{ij,k-\frac{1}{2}}^n} \right) p_{ijk}^{n+1} \right] / h^2,
$$

$$\nabla_h \cdot \mathbf{u}_{ijk}^* = \frac{u_{i+\frac{1}{2},jk}^* - u_{i-\frac{1}{2},jk}^*}{h} + \frac{v_{i,j+\frac{1}{2},k}^* - v_{i,j-\frac{1}{2},k}^*}{h} + \frac{w_{ij,k+\frac{1}{2}}^* - w_{ij,k-\frac{1}{2}}^*}{h}.$$

The Jacobi-type iteration is used to solve Eq. (19). To obtain a unique solution, we take the following pressure correction step after each Jacobi-type iteration:

$$p_{ijk}^{n+1,m+1} = p_{ijk}^{n+1,m+1} - \frac{1}{\#\Omega_\delta^h} \sum_{\mathbf{x}_{ijk} \in \Omega_\delta^h} p_{ijk}^{n+1,m+1},$$

where $\#\Omega_\delta^h$ is the total number of points in Ω_δ^h containing cell centers. The Jacobi-type iteration is applied until the following condition is satisfied with a given tolerance,

$$\| p^{n+1,m+1} - p^{n+1,m} \|_{L^2(\Omega_\delta^h)} < tol,$$

where $p^{n+1,m+1}$ and $p^{n+1,m}$ are the solutions after the $(m+1)$th and mth iterations. Then, let $p^{n+1} = p^{n+1,m+1}$.

Step 4. Finally, compute the updated velocity field.

$$\mathbf{u}^{n+1} = \mathbf{u}^* - \frac{\Delta t}{\rho^n} \nabla_h p^{n+1}. \tag{20}$$

3.1.1. Boundary conditions for pressure and velocity field

When we solve the pressure Poisson equation in a regular domain, the zero-Neumann boundary condition $\nabla p \cdot \mathbf{n} = 0$ is appropriate. In our study, a simple and effective pseudo-Neumann boundary condition is used for the pressure at the ghost points and is defined as

$$p_{ijk} = p(\mathrm{cp}(\mathbf{x}_{ijk})) \text{ for } \mathbf{x}_{ijk} \in \partial\Omega_\delta^h,$$

where

$$\mathrm{cp}(\mathbf{x}_{ijk}) = \mathbf{x}_{ijk} - \frac{\nabla_h d_{ijk}}{|\nabla_h d_{ijk}|^2} d_{ijk}. \tag{21}$$

Because $\mathrm{cp}(\mathbf{x}_{ijk})$ is generally not a grid point, the boundary value $p(\mathrm{cp}(\mathbf{x}_{ijk}))$ is obtained using the trilinear interpolation method. Although our spatial discretization is second-order accurate, the boundary value obtained by a trilinear interpolation is not a strict zero-Neumann boundary, and the computational accuracy may be slightly affected (see the numerical results in Section 4.4). For each $\mathbf{x}_{ijk} \in \partial\Omega_\delta^h$, we compute $\mathrm{cp}(\mathbf{x}_{ijk})$ using Eq. (21) and find the cube cell, $[x_l, x_{l+1}) \times [y_m, y_{m+1}) \times [z_n, z_{n+1})$ containing the point $\mathrm{cp}(\mathbf{x}_{ijk})$. Let $(\alpha_1, \alpha_2, \alpha_3) = \mathrm{cp}(\mathbf{x}_{ijk}) - \mathbf{x}_{lmn}$; then,

$$
\begin{aligned}
p(\mathrm{cp}(\mathbf{x}_{ijk})) = \big[& (h-\alpha_1)(h-\alpha_2)(h-\alpha_3)p_{lmn} + \alpha_1(h-\alpha_2)(h-\alpha_3)p_{l+1,mn} \\
& + (h-\alpha_1)\alpha_2(h-\alpha_3)p_{l,m+1,n} + \alpha_1\alpha_2(h-\alpha_3)p_{l+1,m+1,n} \\
& + (h-\alpha_1)(h-\alpha_2)\alpha_3 p_{lm,n+1} + \alpha_1(h-\alpha_2)\alpha_3 p_{l+1,m,n+1} \\
& + (h-\alpha_1)\alpha_2\alpha_3 p_{l,m+1,n+1} + \alpha_1\alpha_2\alpha_3 p_{l+1,m+1,n+1} \big] / h^3.
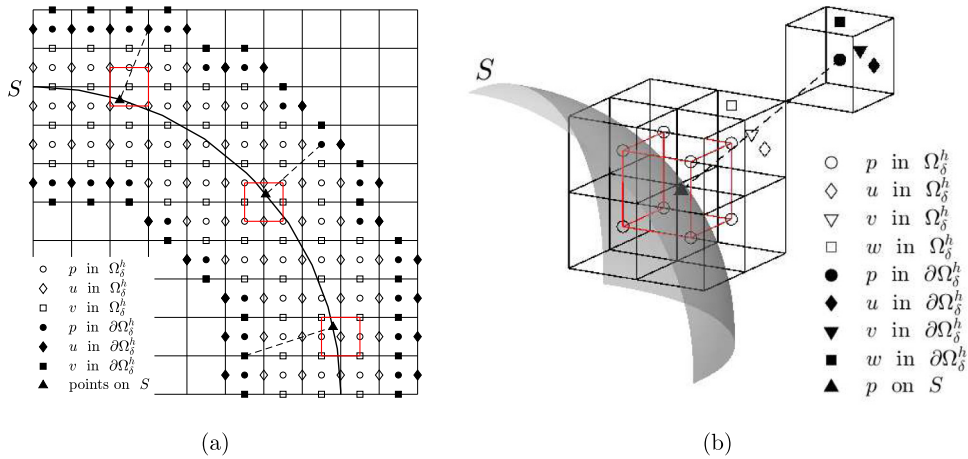\end{aligned} \tag{22}
$$

Fig. 2. Schematic illustrations of trilinear interpolation for the boundary values in (a) two- and (b) three-dimensional spaces.

Schematic illustrations of the interpolation in two- and three-dimensional spaces are shown in Figs. 2(a) and (b), respectively. Note that this type of pseudo-Neumann boundary condition has been successfully applied to various scalar-valued functions on curved surfaces [30,32].

To define the values of the velocity field at ghost points, we consider the following three approaches:

Approach 1. Based on the closest point method, the boundary values of velocities u, v, and w are directly defined by using a similar idea as the pseudo-Neumann boundary condition in Eq. (22) (see Fig. 2), where $u_{i+\frac{1}{2},jk} = u(\mathrm{cpu}(\mathbf{x}_{i+\frac{1}{2},jk}))$ for $\mathbf{x}_{i+\frac{1}{2},jk} \in \partial U_\delta^h$, $v_{i,j+\frac{1}{2},k} = v(\mathrm{cpv}(\mathbf{x}_{i,j+\frac{1}{2},k}))$ for $\mathbf{x}_{i,j+\frac{1}{2},k} \in \partial V_\delta^h$, and $w_{ij,k+\frac{1}{2}} = w(\mathrm{cpw}(\mathbf{x}_{ij,k+\frac{1}{2}}))$ for $\mathbf{x}_{ij,k+\frac{1}{2}} \in \partial W_\delta^h$. The definitions of $u(\mathrm{cpu}(\mathbf{x}_{i+\frac{1}{2},jk}))$, $v(\mathrm{cpv}(\mathbf{x}_{i,j+\frac{1}{2},k}))$, and $w(\mathrm{cpw}(\mathbf{x}_{ij,k+\frac{1}{2}}))$ are as follows:

$$u(\mathrm{cpu}(\mathbf{x}_{i+\frac{1}{2},jk})) = \mathbf{x}_{i+\frac{1}{2},jk} - \frac{\nabla_h U d_{i+\frac{1}{2},jk}}{|\nabla_h U d_{i+\frac{1}{2},jk}|^2} U d_{i+\frac{1}{2},jk},$$

$$v(\mathrm{cpv}(\mathbf{x}_{i,j+\frac{1}{2},k})) = \mathbf{x}_{i,j+\frac{1}{2},k} - \frac{\nabla_h V d_{i,j+\frac{1}{2},k}}{|\nabla_h V d_{i,j+\frac{1}{2},k}|^2} V d_{i,j+\frac{1}{2},k},$$

$$w(\mathrm{cpw}(\mathbf{x}_{ij,k+\frac{1}{2}})) = \mathbf{x}_{ij,k+\frac{1}{2}} - \frac{\nabla_h W d_{ij,k+\frac{1}{2}}}{|\nabla_h W d_{ij,k+\frac{1}{2}}|^2} W d_{ij,k+\frac{1}{2}},$$

where $U d_{i+\frac{1}{2},jk} = 0.5(d_{i+1,jk} + d_{ijk})$, $V d_{i,j+\frac{1}{2},k} = 0.5(d_{i,j+1,k} + d_{ijk})$, and $W d_{ij,k+\frac{1}{2}} = 0.5(d_{ij,k+1} + d_{ijk})$.

Approach 2. From the viewpoint of a Helmholtz–Hodge decomposition, the divergence-free velocity field $\mathbf{u}$ obtained should satisfy $\mathbf{u} \cdot \mathbf{n} = 0$ at the boundary. It is evident that Approach 1 does not satisfy this condition. Instead of directly computing $u(\mathrm{cpu}(\mathbf{x}_{i+\frac{1}{2},jk}))$, $v(\mathrm{cpv}(\mathbf{x}_{i,j+\frac{1}{2},k}))$, and $w(\mathrm{cpw}(\mathbf{x}_{ij,k+\frac{1}{2}}))$ from the interpolations of u, v, and w, we compute the values of $u(\mathrm{cpu}(\mathbf{x}_{i+\frac{1}{2},jk}))$, $v(\mathrm{cpv}(\mathbf{x}_{i,j+\frac{1}{2},k}))$ $w(\mathrm{cpw}(\mathbf{x}_{ij,k+\frac{1}{2}}))$ by using the corrected values $\tilde{u}$, $\tilde{v}$, and $\tilde{w}$, i.e.,

$$\tilde{\mathbf{u}} = \mathbf{u} - (\mathbf{u} \cdot \mathbf{m})\mathbf{m}. \tag{23}$$

where $\tilde{\mathbf{u}} = (\tilde{u}, \tilde{v}, \tilde{w})$ and $\mathbf{u} = (u, v, w)$. The basic idea of this approach is that the velocity field at each ghost point is corrected to be the tangential direction of the curved surface. By using this approach, the boundary velocity normal to the surface is suppressed. The derivation of Eq. (23) is discussed in Approach 3.

Approach 3. When the NS equation is solved on a curved surface, it is desirable to keep the updated velocity field tangential to the surface. Although the velocity field at each ghost point is corrected in Approach 2, the velocity field in the entire narrow band domain is still arbitrarily distributed. To resolve this problem, a correction algorithm for the complete velocity field is used: First, obtain the updated velocity field $\mathbf{u}^{n+1}$ in Step 4 and let $\mathbf{u}^{**} = \mathbf{u}^{n+1}$.
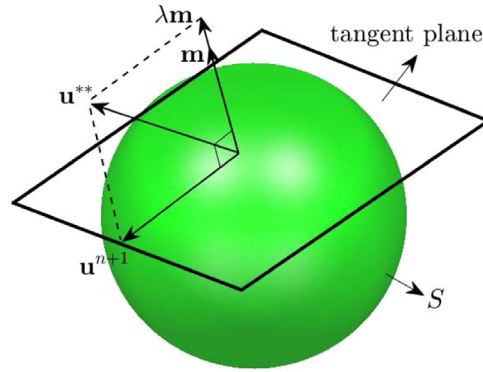
Fig. 3. Schematic illustration of velocity correction step.

Then, let **m** be the unit vector normal to S and $\lambda\mathbf{m}$ be the normal component of $\mathbf{u}^{**}$, i.e., $(\mathbf{u}^{**} - \lambda\mathbf{m}) \cdot \mathbf{m} = \mathbf{0}$, which implies $\lambda = \mathbf{u}^{**} \cdot \mathbf{m}$. The final corrected velocity field is defined as

$$\mathbf{u}^{n+1} = \mathbf{u}^{**} - (\mathbf{u}^{**} \cdot \mathbf{m})\mathbf{m}. \tag{24}$$

Fig. 3 shows a schematic illustration of the velocity correction steps. Note that this approach works as an augmented projection step after Step 4. In each time cycle, Approach 3 corrects the entire velocity field and makes the component of the velocity field normal to the surface almost zero. Owing to this correction, the boundary value of the velocity field can be easily computed using the method in Approach 1, and the condition $\mathbf{u} \cdot \mathbf{n} = 0$ is approximately satisfied at the curved boundary. The numerical test in Section 4 shows that Approach 3 results in the best divergence-free condition among the three approaches.

3.2. Advective Cahn–Hilliard solver

For $\mathbf{x}_{ijk} \in \Omega_\delta^h$, the fully discrete forms of Eqs. (12) and (13) are written as follows:

$$\frac{\phi_{ijk}^{n+1} - \phi_{ijk}^n}{\Delta t} + \nabla_h \cdot (\mathbf{u}\phi)_{ijk}^n = \Delta_h \mu_{ijk}^{n+1},$$
$$\mu_{ijk}^{n+1} = (\phi_{ijk}^{n+1})^3 - \phi_{ijk}^n - Cn^2 \Delta_h \phi_{ijk}^{n+1}, \tag{25}$$

where the standard seven-point Laplace operator for ϕ is defined as $\Delta_h \phi_{ijk} = (\phi_{i+1,jk} + \phi_{i-1,jk} + \phi_{i,j+1,k} + \phi_{i,j-1,k} + \phi_{ij,k+1} + \phi_{ij,k-1} - 6\phi_{ijk})/h^2$. The conservative scheme of the advection term in Eq. (25) is defined as follows [54]:

$$\nabla_h \cdot (\phi\mathbf{u})_{ijk} = ((\phi u)_x + (\phi v)_y + (\phi w)_z)_{ijk}$$
$$= \frac{u_{i+\frac{1}{2},jk}(\phi_{i+1,jk} + \phi_{ijk}) - u_{i-\frac{1}{2},jk}(\phi_{ijk} + \phi_{i-1,jk})}{2h}$$
$$+ \frac{v_{i,j+\frac{1}{2},k}(\phi_{i,j+1,k} + \phi_{ijk}) - v_{i,j-\frac{1}{2},k}(\phi_{ijk} + \phi_{i,j-1,k})}{2h}$$
$$+ \frac{w_{ij,k+\frac{1}{2}}(\phi_{ij,k+1} + \phi_{ijk}) - w_{ij,k-\frac{1}{2}}(\phi_{ijk} + \phi_{ij,k-1})}{2h}.$$

The pseudo-Neumann boundary conditions are used for ϕ and μ. For the given values ϕ_{ijk}^n and μ_{ijk}^n, we compute ϕ_{ijk}^{n+1} and μ_{ijk}^{n+1} by iterating the following Eqs. (26) and (27) until the stopping criterion is satisfied, i.e., $\|\phi^{n+1,m+1} - \phi^{n+1,m}\|_{L^2(\Omega_\delta^h)} < tol$. Because $(\phi_{ijk}^{n+1})^3$ is nonlinear with respect to ϕ_{ijk}^n, the following Newtonian-type linearization is used in the iterations:

$$(\phi_{ijk}^{n+1,m+1})^3 \approx (\phi_{ijk}^{n+1,m})^3 + 3(\phi_{ijk}^{n+1,m})^2(\phi_{ijk}^{n+1,m+1} - \phi_{ijk}^{n+1,m}),$$

where $\phi^{n+1,m}$ and $\phi^{n+1,m+1}$ are the results after the mth and $(m+1)$th rounds of Jacobi-type iterations.

$$
\begin{aligned}
&\frac{\phi_{ijk}^{n+1,m+1}}{\Delta t} + \frac{6\mu_{ijk}^{n+1,m+1}}{Peh^2} = \frac{\phi_{ijk}^n}{\Delta t} - \nabla_h \cdot (\phi\mathbf{u})_{ijk}^n \\
&+ \frac{\mu_{i+1,jk}^{n+1,m} + \mu_{i-1,jk}^{n+1,m} + \mu_{i,j+1,k}^{n+1,m} + \mu_{i,j-1,k}^{n+1,m} + \mu_{ij,k+1}^{n+1,m} + \mu_{ij,k-1}^{n+1,m}}{Peh^2},
\end{aligned}
\tag{26}
$$

$$
- \left[3(\phi_{ijk}^{n+1,m})^2 + \frac{6Cn^2}{h^2} \right] \phi_{ijk}^{n+1,m+1} + \mu_{ijk}^{n+1,m+1} = -\phi_{ijk}^n - 2(\phi_{ijk}^{n+1,m})^3
$$

$$
- \frac{Cn^2}{h^2} \left(\phi_{i+1,jk}^{n+1,m} + \phi_{i-1,jk}^{n+1,m} + \phi_{i,j+1,k}^{n+1,m} + \phi_{i,j-1,k}^{n+1,m} + \phi_{ij,k+1}^{n+1,m} + \phi_{ij,k-1}^{n+1,m} \right).
\tag{27}
$$

3.2.1. Mass correction step

The mass conservation is a basic property of the CH model. However, because it is not a strict zero-Neumann boundary condition in a finite difference framework, the pseudo-Neumann boundary condition may cause a nonphysical mass loss. To correct the mass loss, an effective mass correction algorithm [55] is used, which is briefly described in the method as follows. For the conservative CH model, we require

$$
\frac{1}{\#\Omega_\delta^h} \sum_{\mathbf{x}_{ijk} \in \Omega_\delta^h} \phi_{ijk}^{n+1} = \frac{1}{\#\Omega_\delta^h} \sum_{\mathbf{x}_{ijk} \in \Omega_\delta^h} \phi_{ijk}^n = \cdots = \frac{1}{\#\Omega_\delta^h} \sum_{\mathbf{x}_{ijk} \in \Omega_\delta^h} \phi_{ijk}^0.
\tag{28}
$$

If the converged solution of Eqs. (26) and (27) is $\tilde{\phi}_{ijk}^{n+1}$, then let $\phi_{ijk}^{n+1} = \tilde{\phi}_{ijk}^{n+1} + \mathcal{L}\sqrt{F(\tilde{\phi}_{ijk}^{n+1})}$. The auxiliary multiplier can be calculated as follows to satisfy Eq. (28):

$$
\mathcal{L} = \sum_{\mathbf{x}_{ijk} \in \Omega_\delta^h} \left(\phi_{ijk}^0 - \tilde{\phi}_{ijk}^{n+1} \right) / \sum_{\mathbf{x}_{ijk} \in \Omega_\delta^h} \sqrt{F(\tilde{\phi}_{ijk}^{n+1})}.
\tag{29}
$$

Thus, the corrected phase variable is expressed as follows:

$$
\phi_{ijk}^{n+1} = \tilde{\phi}_{ijk}^{n+1} + \frac{\sum_{\mathbf{x}_{ijk} \in \Omega_\delta^h} \left(\phi_{ijk}^0 - \tilde{\phi}_{ijk}^{n+1} \right)}{\sum_{\mathbf{x}_{ijk} \in \Omega_\delta^h} \sqrt{F(\tilde{\phi}_{ijk}^{n+1})}} \sqrt{F(\tilde{\phi}_{ijk}^{n+1})}.
\tag{30}
$$

Further details on this technique can be found in [55].

Remarks. In our approach, an effective pseudo-Neumann boundary condition is used. The boundary values are calculated from the interpolation technique. Although this technique is easy and practical for defining the boundary values, the pseudo-Neumann boundary condition is not a strict zero-Neumann boundary condition, and thus it is difficult to analytically prove the energy stability of the entire system. However, the numerical results in Section 4 show that the discrete energy dissipation can still be obtained for various complex 3D surfaces. Furthermore, we only focus on the implementation of our method for the fluid flows on various curved surfaces. For convenience, a first-order temporal discretization is used and the classical projection method is adopted for solving the NS equation. Note that the second-order temporal schemes and the recently developed fluid model with large density ratios [4,21] may be more interesting, and our proposed method can be directly applied to these schemes and models. However, this will be covered in a future study.

4. Numerical experiments

We conduct various numerical tests to show the effectiveness and accuracy of the proposed method. The single fluid flows on a sphere and torus surfaces are considered to show the divergence-free condition and effectiveness. Then, standard two-phase fluid flows, such as the Kelvin–Helmholtz instability, hydrodynamic coarsening, and Rayleigh–Taylor instability, are investigated on various 3D surfaces. In all simulations, the initial velocity field and phase variable are defined in the narrow band domains $U_\delta \cup V_\delta \cup W_\delta$ and Ω_δ, respectively. Unless otherwise specified, the viscosity-matched condition, i.e., $\eta_1 : \eta_2 = 1 : 1$ is used.
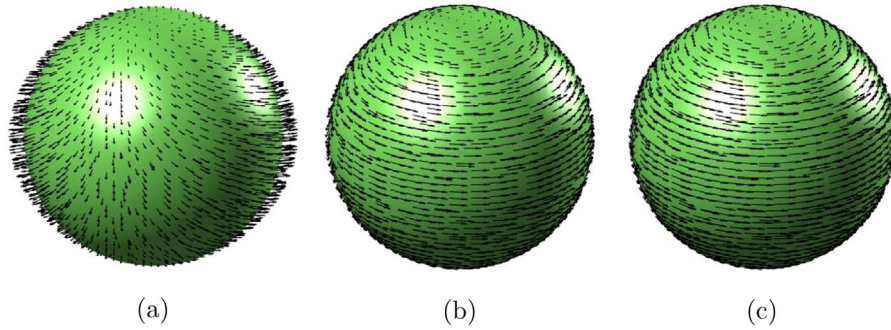
Fig. 4. Circulation flow on the sphere with respect to Approaches (a) 1, (b) 2, and (c) 3. The images are taken at $t = 2.67$.

Table 1
Values of $\overline{Div}$ obtained by Approach 3 at some specific moments.

Time	$\overline{Div}$	Time	$\overline{Div}$	Time	$\overline{Div}$
t = 0.27	2.20e−3	t = 1.20	1.90e−3	t = 1.93	1.60e−3
t = 0.53	2.10e−3	t = 1.33	1.80e−3	t = 2.00	1.60e−3
t = 0.67	2.10e−3	t = 1.47	1.80e−3	t = 2.13	1.60e−3
t = 0.87	2.00e−3	t = 1.60	1.70e−3	t = 2.33	1.50e−3
t = 1.00	1.90e−3	t = 1.80	1.70e−3	t = 2.67	1.40e−3

4.1. Divergence-free test

A divergence-free condition is an important property of an incompressible NS equation. It is well known that the classical projection method based on the Helmholtz–Hodge decomposition can satisfy the divergence-free condition in theory. However, in actual computations, improper boundary conditions of the velocity field can significantly affect the numerical results of an intermediate velocity field and pressure Poisson equation, and can then violate the discrete divergence-free condition. In Section 3.1.1, we proposed three types of approaches for defining the velocity boundary conditions. To test the practicability of those three approaches, we consider the circulation flow on a sphere in the domain $\Omega = (-1, 1)^3$. The signed distance function is $d(x, y, z) = \sqrt{x^2 + y^2 + z^2} - 0.6$. The initial velocity fields are defined as

$$u(x, y, z, 0) = -y, \quad v(x, y, z, 0) = x, \quad w(x, y, z, 0) = 0. \tag{31}$$

The parameters applied are as follows: $h = 0.033$, $\Delta t = 0.2h^2$, $Re = 50$, and $tol = 10^{-3}$. The images at $t = 2.67$ are shown in Figs. 4(a), (b), and (c) with respect to Approaches 1, 2, and 3, respectively. It is evident that Approach 1 causes a nonphysical evolution of the velocity field. Both Approaches 2 and 3 lead to the desired circulation flow on the surface. To quantitatively investigate the divergence-free condition, we define the average discrete divergence as follows:

$$\overline{Div} = \frac{1}{\#\Omega_\delta^h} \sum_{\mathbf{x}_{ijk} \in \, \Omega_\delta^h} \left| \frac{u_{i+\frac{1}{2}, jk} - u_{i-\frac{1}{2}, jk}}{h} + \frac{v_{i, j+\frac{1}{2}, j} - v_{i, j-\frac{1}{2}, k}}{h} + \frac{w_{ij, k+\frac{1}{2}} - w_{ij, k-\frac{1}{2}}}{h} \right|,$$

where Ω_δ^h is the discrete narrow band domain containing all cell centers and $\#\Omega_\delta^h$ is the total number of points in Ω_δ^h. In Fig. 5, we plot the temporal evolutions of $\overline{Div}$ with respect to the three approaches. Table 1 lists the values of $\overline{Div}$ obtained by Approach 3 at some specific moments. As we can see, Approach 3 approximately satisfies the discrete divergence-free condition in a lengthy simulation. Thus, Approach 3 is used in the numerical calculation of the NS equation.

4.2. Tolerance test

In all simulations, the stopping tolerance of the iterations for the pressure Poisson equation is set as $tol = 10^{-3}$. To verify whether this tolerance is sufficiently small in the present study, we chose three different tolerances:
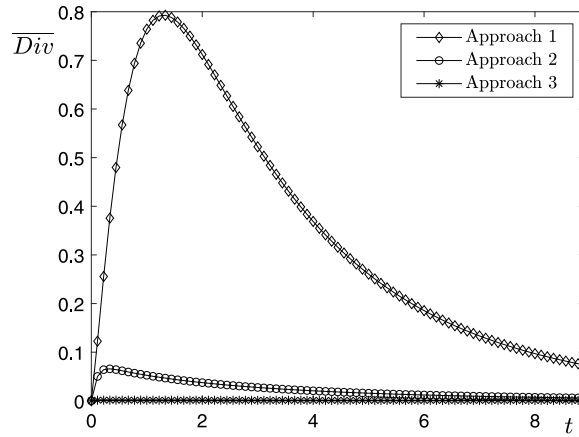
Fig. 5. Temporal evolutions of discrete divergence with respect to the three approaches.
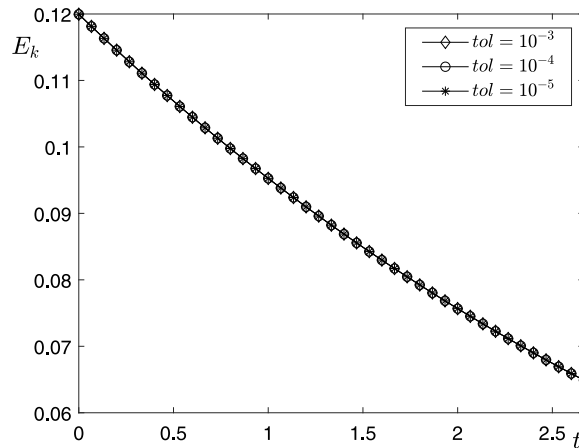

Fig. 6. Temporal evolutions of discrete kinetic energy with respect to different tolerances.

$tol = 10^{-3}, 10^{-4}$, and 10^{-5} to test the dissipation of the total kinetic energy, which is a basic property of the NS equation. The initial conditions and computational domain were set to be the same as those in Section 4.1. The discrete total kinetic energy is defined as follows:

$$E_k = \frac{\rho}{2} \left[\frac{1}{2} \sum_{\mathbf{x}_{ijk} \in \ \Omega_\delta^h} \left(u_{i+\frac{1}{2},jk}^2 + u_{i-\frac{1}{2},jk}^2 \right) + \frac{1}{2} \sum_{\mathbf{x}_{ijk} \in \ \Omega_\delta^h} \left(v_{i,j+\frac{1}{2},k}^2 + v_{i,j-\frac{1}{2},k}^2 \right) \right.$$
$$\left. + \frac{1}{2} \sum_{\mathbf{x}_{ijk} \in \ \Omega_\delta^h} \left(w_{ij,k+\frac{1}{2}}^2 + w_{ij,k-\frac{1}{2}}^2 \right) \right] h^3, \tag{32}$$

where $\rho = 1$ is used. Note that the above weighted summations have been extensively used in previous studies [21,56]. In Fig. 6, we plot the temporal evolution of E_k with respect to different tolerances and almost the same results can be observed, which indicates that $tol = 10^{-3}$ is sufficiently small to obtain accurate solutions. Thus, in the following tests, $tol = 10^{-3}$ is used, unless otherwise specified.
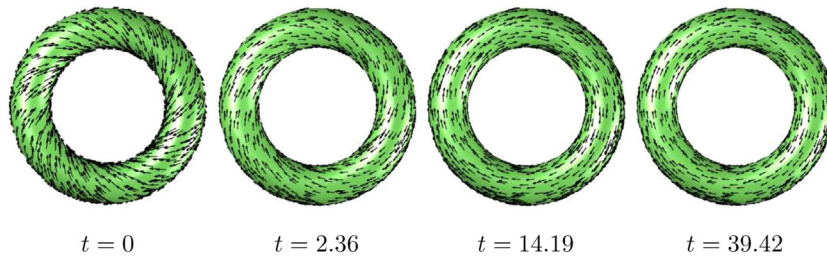
$t = 0$ $\qquad$ $t = 2.36$ $\qquad$ $t = 14.19$ $\qquad$ $t = 39.42$

Fig. 7. Single fluid flow on a torus.

Table 2
Comparison with the previous results [36,37]. Here, $|\mathbf{u}|_{min}$ and $|\mathbf{u}|_{max}$ are the minimum and maximum magnitudes of the velocity field, respectively.

	Previous	Present
$|\mathbf{u}|_{min}$	0.02	0.0203
$|\mathbf{u}|_{max}$	0.12	0.1232

4.3. Flow on a torus

To verify the practicability of the proposed method, we consider the fluid flow on a torus embedded in $\Omega = (-4, 4)^3$. The signed distance function of a torus is $d(x, y, z) = \sqrt{(\sqrt{x^2 + y^2} - 2)^2 + z^2} - 0.5$. The initial velocity field is given by

$$u(x, y, z, 0) = \frac{y - 2xz}{8(x^2 + y^2)}, \quad v(x, y, z, 0) = \frac{-x - 2yz}{8(x^2 + y^2)}, \quad w(x, y, z, 0) = \frac{\sqrt{x + y} - 2}{4(\sqrt{x^2 + y^2})}.$$

The following numerical parameters are used: $h = 0.067$, $\Delta t = 0.25h^2$, and $Re = 50$. We show the images at different computational moments in Fig. 7, and can see that the initial velocity field evolves into a circulation flow over time. Note that similar phenomena were observed in the previous studies [36,37], in which the authors investigated the minimum and maximum magnitudes of the velocity field on a torus. Table 2 indicates that the previous and present results are in good agreement.

4.4. Accuracy test for two-phase system

To estimate the spatial and temporal convergence rates, we consider the two-phase fluid system on a sphere with the following signed distance function $d(x, y, z) = \sqrt{x^2 + y^2 + z^2} - 0.8$. The full domain is $\Omega = (-2, 2)^3$. The initial conditions are defined as

$$\phi(x, y, z, 0) = \tanh\left(\frac{0.5 - \sqrt{(x - 0.8)^2 + y^2 + z^2}}{\sqrt{2}\epsilon}\right),$$

$$u(x, y, z, 0) = -y, \quad v(x, y, z, 0) = x, \quad w(x, y, z, 0) = 0.$$

The simulations are performed by varying $h = 0.44$, 0.22, 0.11, and 0.055. The time step is $\Delta t = 0.001h^2$ and the other numerical parameters are as follows: $Re = 10$, $\epsilon = 0.24$, $Cn = \epsilon$, and $Pe = 1$. The effects of the surface tension and gravity are ignored. The successive error for ϕ between two different mesh sizes is defined as follows:

$$e_{ijk}^{\phi} = \phi_{ijk}^{h, \Delta t} - \frac{1}{8}\left(\phi_{2i,2j,2k}^{h/2, \Delta t/4} + \phi_{2i-1,2j,2k}^{h/2, \Delta t/4} + \phi_{2i,2j-1,2k}^{h/2, \Delta t/4} + \phi_{2i,2j,2k-1}^{h/2, \Delta t/4}\right.$$
$$\left. + \phi_{2i-1,2j-1,2k}^{h/2, \Delta t/4} + \phi_{2i,2j-1,2k-1}^{h/2, \Delta t/4} + \phi_{2i-1,2j,2k-1}^{h/2, \Delta t/4} + \phi_{2i-1,2j-1,2k-1}^{h/2, \Delta t/4}\right).$$

In addition, the successive errors for u, v, and w between two different mesh sizes are defined as follows:

$$e_{i+\frac{1}{2}, jk}^{u} = u_{i+\frac{1}{2}, jk}^{h, \Delta t} - \frac{1}{4}\left(u_{2i+\frac{1}{2},2j,2k}^{h/2, \Delta t/4} + u_{2i+\frac{1}{2},2j-1,2k}^{h/2, \Delta t/4} + u_{2i+\frac{1}{2},2j,2k-1}^{h/2, \Delta t/4} + u_{2i+\frac{1}{2},2j-1,2k-1}^{h/2, \Delta t/4}\right),$$

Table 3
Errors and convergence rates with different mesh sizes at $t = 3.95\text{e-}4$.

h	$0.44 - 0.22$		$0.22 - 0.11$		$0.11 - 0.055$
L_2-error: ϕ	0.865		0.243		0.066
rate:		1.832		1.880	
L_2-error: u	1.808		0.412		0.131
rate:		2.134		1.653	
L_2-error: v	1.975		0.496		0.133
rate:		1.993		1.899	
L_2-error: w	5.5e$-$3		1.6e$-$3		3.390e$-$4
rate:		1.781		2.239	

$$e^v_{i,j+\frac{1}{2},k} = v^{h,\Delta t}_{i,j+\frac{1}{2},k} - \frac{1}{4}\left(v^{h/2,\Delta t/4}_{2i,2j+\frac{1}{2},2k} + v^{h/2,\Delta t/4}_{2i-1,2j+\frac{1}{2},2k} + v^{h/2,\Delta t/4}_{2i,2j+\frac{1}{2},2k-1} + v^{h/2,\Delta t/4}_{2i-1,2j+\frac{1}{2},2k-1}\right),$$

$$e^w_{ij,k+\frac{1}{2}} = w^{h,\Delta t}_{ij,k+\frac{1}{2}} - \frac{1}{4}\left(w^{h/2,\Delta t/4}_{2i,2j,2k+\frac{1}{2}} + w^{h/2,\Delta t/4}_{2i-1,2j,2k+\frac{1}{2}} + w^{h/2,\Delta t/4}_{2i,2j-1,2k+\frac{1}{2}} + w^{h/2,\Delta t/4}_{2i-1,2j-1,2k+\frac{1}{2}}\right).$$

We define the L^2-error for ϕ as

$$\|\phi^{h,\Delta t} - \phi^{h/2,\Delta t/4}\|_{L^2(\Omega^h_\delta)} = \sqrt{\sum_{\mathbf{x}_{ijk}\in\,\Omega^h_\delta}(e^\phi_{ijk})^2 h^3}.$$

In addition, the weighted L^2-errors for u, v, and w are defined as

$$\|u^{h,\Delta t} - u^{h/2,\Delta t/4}\|_{L^2(\Omega^h_\delta)} = \sqrt{\sum_{\mathbf{x}_{ijk}\in\,\Omega^h_\delta}\frac{1}{2}\left((e^u_{i+\frac{1}{2},jk})^2 + (e^u_{i-\frac{1}{2},jk})^2\right)h^3},$$

$$\|v^{h,\Delta t} - v^{h/2,\Delta t/4}\|_{L^2(\Omega^h_\delta)} = \sqrt{\sum_{\mathbf{x}_{ijk}\in\,\Omega^h_\delta}\frac{1}{2}\left((e^v_{i,j+\frac{1}{2},k})^2 + (e^v_{i,j-\frac{1}{2},k})^2\right)h^3},$$

$$\|w^{h,\Delta t} - w^{h/2,\Delta t/4}\|_{L^2(\Omega^h_\delta)} = \sqrt{\sum_{\mathbf{x}_{ijk}\in\,\Omega^h_\delta}\frac{1}{2}\left((e^w_{ij,k+\frac{1}{2}})^2 + (e^w_{ij,k-\frac{1}{2}})^2\right)h^3}.$$

The convergence rate for ϕ is defined as

$$\text{rate} = \log_2\left(\frac{\|\phi^{h,\Delta t} - \phi^{h/2,\Delta t/4}\|_{L^2(\Omega^h_\delta)}}{\|\phi^{h/2,\Delta t/4} - \phi^{h/4,\Delta t/16}\|_{L^2(\Omega^{h/2}_\delta)}}\right).$$

The convergence rates for u, v, and w are similarly defined. The simulations are performed until $t = 3.95\text{e-}4$. We list the errors and convergence rates in Table 3. The results show that the proposed scheme has approximately second-order accuracy in space and first-order accuracy in time. Note that we used the pseudo-Neumann boundary condition and computed the boundary values by interpolations, and the accuracy of the numerical results may be slightly affected by this implementation.

4.5. Kelvin–Helmholtz instability on a sphere

The Kelvin–Helmholtz instability is a typical example of two-phase fluid flow [57]. When a difference in velocity exists at the interface of two different fluids, a small disturbance develops there over time and the interface rolls up to form a vortex shape. This well-known fluid instability can be used to describe the formations of various natural phenomena, such as a billow cloud. To investigate the formation of the Kelvin–Helmholtz instability on a sphere,
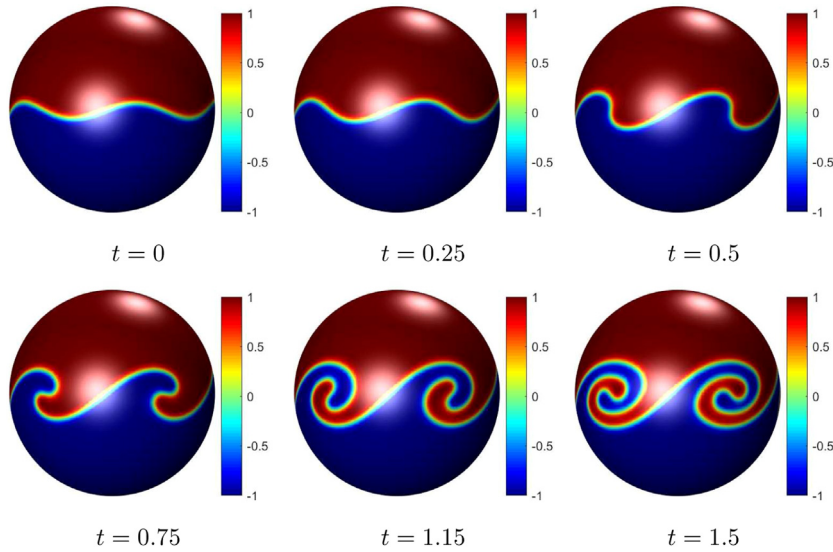
Fig. 8. Kelvin–Helmholtz instability on a sphere. The colorbars reflect the value of ϕ. (For interpretation of the references to color in this figure legend, the reader is referred to the web version of this article.)
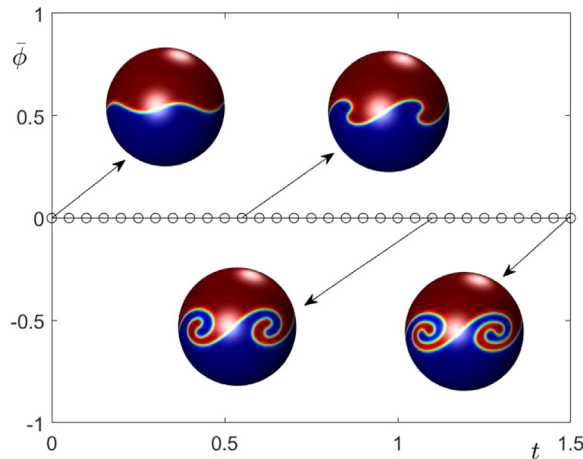

Fig. 9. Temporal evolution of average concentration of Kelvin–Helmholtz instability. The insets are images corresponding to the specific computational moments.

we consider the following initial conditions:

$$\phi(x, y, z, 0) = \tanh\left(\frac{-R\theta + 0.5R\pi + 0.06\cos(5\psi)}{\sqrt{2}\epsilon}\right),$$

$$u(x, y, z, 0) = \phi(x, y, z, 0)y, \quad v(x, y, z, 0) = -\phi(x, y, z, 0)x, \quad w(x, y, z, 0) = 0,$$

where $R = 0.8$ is the radius of a sphere, $\theta = \cos^{-1}(z/r)$, $\psi = \tan^{-1}(y, x)$ with $x \neq 0$, and $r = \sqrt{x^2 + y^2 + z^2}$. The signed distance function $d(x, y, z) = \sqrt{x^2 + y^2 + z^2} - R$ is defined in $\Omega = (-1, 1)^3$. During the simulation, we consider $h = 0.025$, $\Delta t = 0.4h^2$, $Re = 5000$, $\epsilon = 0.024$, $Cn = \epsilon$, and $Pe = 1/\epsilon$. The effects of the surface tension and gravity are omitted. We display the images at different computational moments in Fig. 8.

For a two-phase incompressible flow, mass conservation is an important issue. We plot the temporal evolution of the average concentration $\bar{\phi} = \frac{1}{\#\Omega_\delta^h}\sum_{\mathbf{x}_{ijk} \in \Omega_\delta^h} \phi_{ijk}^n$ in Fig. 9. As evident from the figure, the mass conservation is well satisfied by our proposed method.
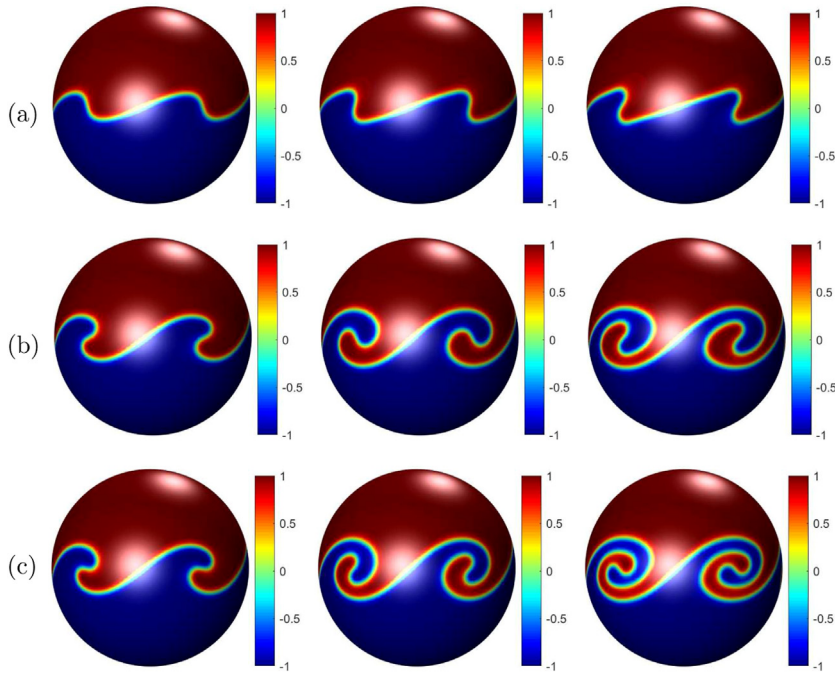
Fig. 10. Images of the Kelvin–Helmholtz instability with respect to different Reynolds numbers: (a) $Re = 50$, (b) $Re = 500$, and (c) $Re = 5000$. The images from left to right in each row are taken at $t = 0.75$, 1.15, and 1.5, respectively. The colorbars reflect the value of ϕ. (For interpretation of the references to color in this figure legend, the reader is referred to the web version of this article.)

The Reynolds number Re plays an important role in fluid dynamics, and we will now briefly investigate the effect of Re on the dynamics of a two-phase Kelvin–Helmholtz instability. Three different values of Reynolds number, $Re = 50$, 500, and 5000, are considered in the simulations. The evolutions with respect to different Re are displayed in Fig. 10. We can see that the roll-up is further developed with the increase in Re. When Re is small, the effect of the fluid viscosity is dominant, which significantly suppresses the evolution of the interface.

4.6. Effect of viscosity ratio

To show the effect of the viscosity ratio on the dynamics of a two-phase flow on a curved surface, we consider the Kelvin–Helmholtz instability on a sphere with the same initial conditions and parameters as in Section 4.5. Figs. 11(a), (b), and (c) display the images of the Kelvin–Helmholtz instability with respect to different viscosity ratios: $\eta_1 : \eta_2 = 1 : 1$, 1 : 5, and 1 : 10, respectively. With an increase in the viscosity of fluid 2, the interfacial dynamics are suppressed.

4.7. Coarsening dynamics

To demonstrate the dissipation of the total energy of the NSCH model, we consider the coarsening dynamics on 3D surfaces in the presence of a fluid flow. The domain is $\Omega = (-2, 2)^3$, and a signed distance function, $d_1(x, y, z) = \sqrt{x^2 + y^2 + z^2} - 1.6$ and a scalar function, $d_2(x, y, z) = (x^2 + y^2 - 1)^2 + (x^2 + z^2 - 1)^2 + (y^2 + z^2 - 1)^2 + (x^2 - 1)^2 + (y^2 - 1)^2 + (z^2 - 1)^2 - 2$ are used. The initial phase variable is defined randomly, i.e., $\phi(x, y, z, 0) = 0.5\text{rand}(x, y, z)$, where rand (x, y, z) is a random number between -1 and 1. The initial velocity field is set to zero. We use $h = 0.067$ as the spatial step. The following parameters are used: $\Delta t = 0.2h^2$, $Re = 100$, $\epsilon = 0.064$, $Pe = 1$, $Cn = \epsilon$, and $Bo = 1/Cn$. The effect of gravity is not considered. The results at different computational moments are shown in
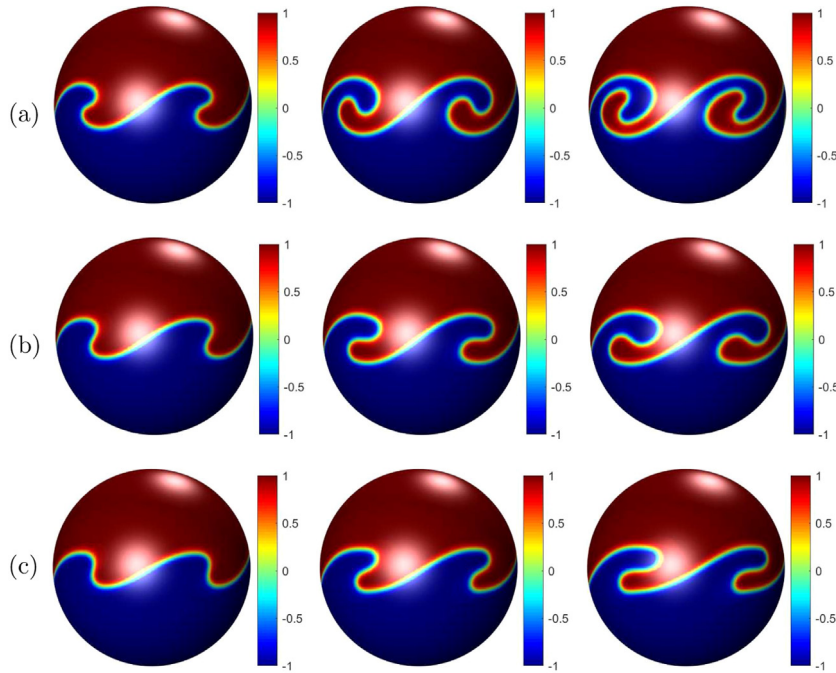
Fig. 11. Images of Kelvin–Helmholtz instability with respect to different viscosity ratios: (a) $\eta_1 : \eta_2 = 1 : 1$, (b) $\eta_1 : \eta_2 = 1 : 5$, and (c) $\eta_1 : \eta_2 = 1 : 10$. The images from the left to right in each row are taken at $t = 0.75$, 1.15, and 1.5. The colorbars reflect the value of ϕ. (For interpretation of the references to color in this figure legend, the reader is referred to the web version of this article.)

Fig. 12, and we can see that the phase separates over time. We define the discrete total energy E_t as follows:

$$
E_t = \sum_{\mathbf{x}_{ijk} \in \, \Omega_\delta^h} \left[\frac{Cn^2}{2} \left(\frac{(\phi_{i+1,jk} - \phi_{ijk})^2}{h^2} + \frac{(\phi_{i,j+1,k} - \phi_{ijk})^2}{h^2} \right. \right.
$$

$$
\left. \left. + \frac{(\phi_{ij,k+1} - \phi_{ijk})^2}{h^2} \right) + F(\phi_{ijk}) \right] h^3 + E_k,
$$

where E_k is the total discrete kinetic energy defined in Section 4.2. The temporal evolutions of the discrete total energy on Ω_1 and Ω_2 are shown in Figs. 13(a) and (b), respectively, and we can see that the energy is non-increasing on a 3D surface.

4.8. Rayleigh–Taylor instability on a sphere

When a heavier fluid is located above another lighter fluid, a small disturbance on the interface will cause the heavier fluid to roll and fall, forming a spike structure, whereas the lighter fluid floats up to form a bubble. This phenomenon is called the Rayleigh–Taylor instability [15,54], which is an important buoyancy-driven two-phase flow problem appearing in various scientific and industrial fields. In a three-dimensional space, we know that the direction of gravitation force $\mathbf{g} = (0, 0, -1)$ is always downward. To consider the gravitational effect on the arbitrarily curved surface, we use the same correction step as in Section 3.1.1 to treat the gravity field, i.e.,

$$
\mathbf{g}^* = \mathbf{g} - (\mathbf{g} \cdot \mathbf{m})\mathbf{m},
$$

where $\mathbf{m}$ is the unit vector normal to the surface, and $\mathbf{g}^*$ is an effective gravity field tangential to the surface. The signed distance function is $d(x, y, z) = \sqrt{x^2 + y^2 + z^2} - 0.8$. The same initial conditions as in Section 4.5 are used. The numerical parameters are as follows: $h = 0.025$, $\Delta t = 4h^2$, $Re = 3000$, $\epsilon = 0.024$, $Pe = 1/\epsilon$, $Cn = \epsilon$, $\rho_1 : \rho_2 = 3 : 1$, and $Fr = 0.58$. The surface tension is ignored, i.e., $Bo = \infty$. From the results in Fig. 14, the roll-up of a heavier fluid can be clearly observed.
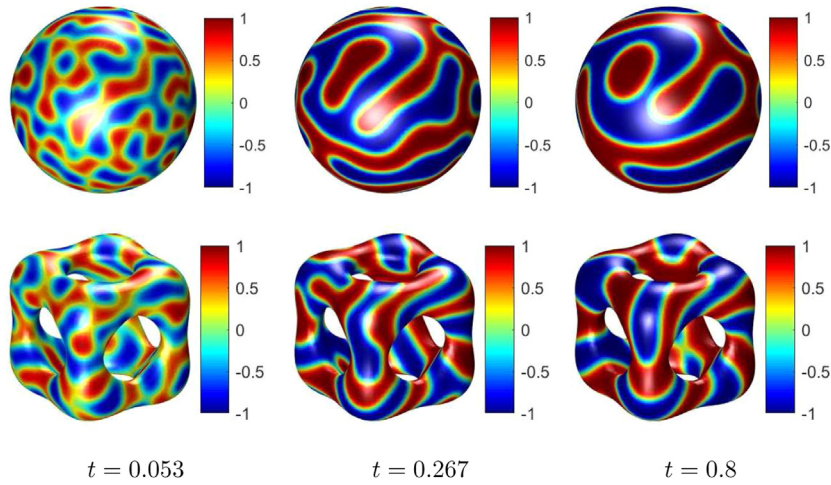
$t = 0.053$ $t = 0.267$ $t = 0.8$

Fig. 12. Coarsening dynamics on curved surfaces. The colorbars reflect the value of ϕ. (For interpretation of the references to color in this figure legend, the reader is referred to the web version of this article.)
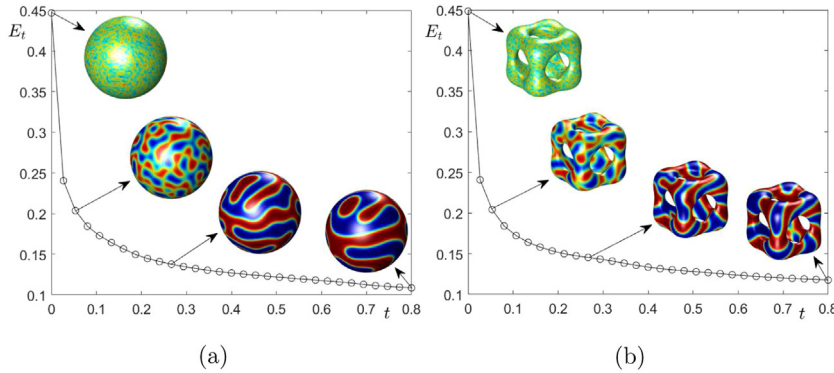

(a)   (b)

Fig. 13. Temporal evolutions of the discrete total energy on a curved surface.

4.9. Buoyancy-driven flow on a bunny surface

To verify that the proposed method can be used to simulate a two-phase fluid flow on a more complex surface, we consider the buoyancy-driven flow on a bunny surface embedded in $\Omega = (0, 69)^3$. The initial conditions are defined as follows:

$$\phi(x, y, z, 0) = \tanh\left(\frac{z - 34.5 + 0.06 \text{rand}(x, y, z)}{\sqrt{2}\epsilon}\right),\tag{33}$$

$$u(x, y, z, 0) = v(x, y, z, 0) = w(x, y, z, 0) = 0.\tag{34}$$

The following numerical parameters are used: $h = 0.5$, $\Delta t = 0.1h^2$, $Re = 3000$, $\epsilon = 0.48$, $Pe = 0.42$, $Cn = \epsilon$, $\rho_1 : \rho_2 = 3 : 1$, and $Fr = 0.58$. We do not consider the effect of the surface tension. The numerical results shown in Fig. 15 indicate that the proposed method can be effectively used for simulating a two-phase flow with gravitational force on a complex surface.

5. Conclusions

In this paper, we presented a phase-field model and its efficient numerical method for the incompressible single and binary fluid flows on arbitrarily curved surfaces in a three-dimensional space. The incompressible two-phase fluid flow is governed by the NSCH system. In the proposed method, we used a narrow band domain to embed the
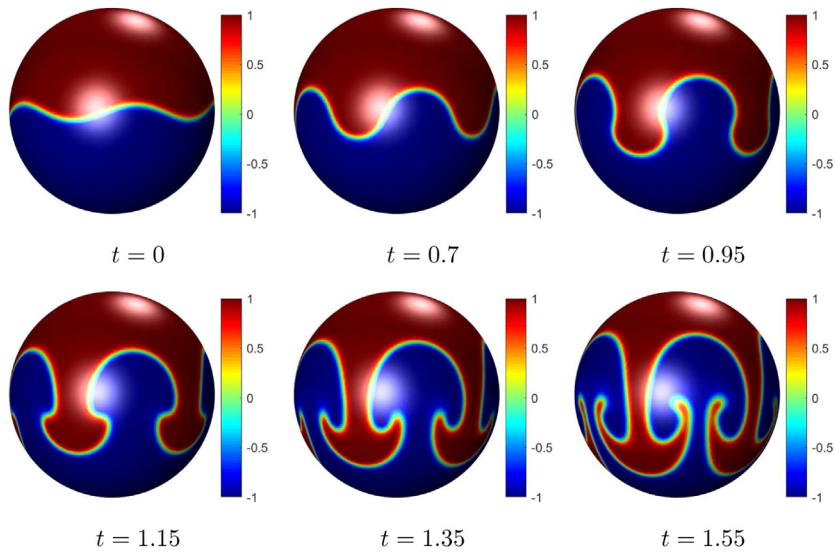
Fig. 14. The Rayleigh–Taylor instability on a sphere. The colorbars reflect the value of ϕ. (For interpretation of the references to color in this figure legend, the reader is referred to the web version of this article.)
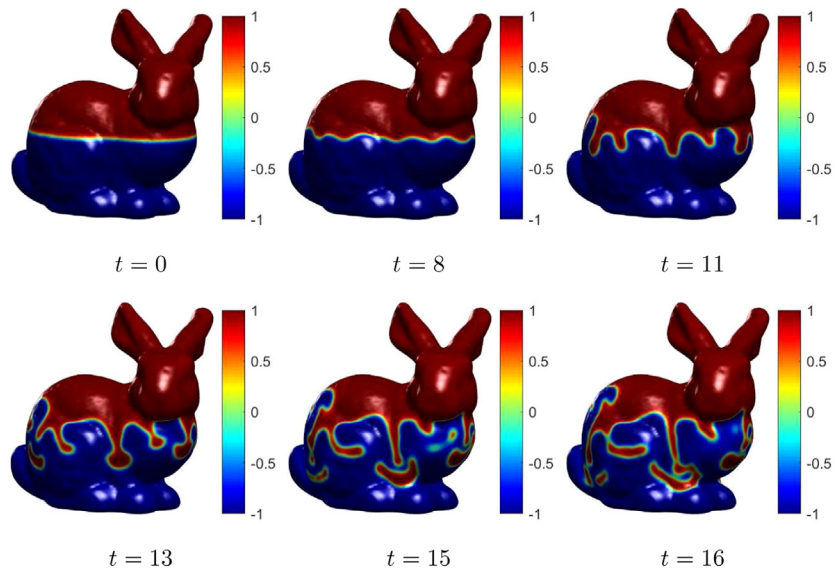

Fig. 15. The buoyancy-driven flow on a bunny surface. The colorbars reflect the value of ϕ. (For interpretation of the references to color in this figure legend, the reader is referred to the web version of this article.)

arbitrarily curved surface and extended the NSCH system to the narrow band domain. We used a pseudo-Neumann boundary condition on the boundary of the narrow band domain, which enforces the dependent variables to be constant along the normal direction of the points on the surface. We can therefore use the standard discrete Laplace operator instead of the discrete Laplace–Beltrami operator. The Chorin's projection method was applied to solve the NS equation and a convex splitting method was employed to solve the CH equation with an advection term. To make the velocity field tangential to the surface, a velocity correction procedure was applied. An effective mass correction step was adopted to preserve the phase concentration. Computational results such as a convergence test, Kevin–Helmholtz instability, and Rayleigh–Taylor instability on curved surfaces demonstrated the accuracy and efficiency of the proposed method. Note that the proposed method can be used to study arbitrary N-component

($N \geq 3$) incompressible fluid flows or a hydrodynamically coupled surfactant system on 3D curved surfaces. Furthermore, our method will be extended to simulate multi-phase flow phenomena on the surfaces of planets.

Declaration of competing interest

The authors declare that they have no known competing financial interests or personal relationships that could have appeared to influence the work reported in this paper.

Acknowledgments

Appendix

We briefly describe the discrete advection terms for v and w. We discretize the advection term in Eq. (15) as follows:

$$
\begin{aligned}
(\mathbf{u} \cdot \nabla_h v)_{i,j+\frac{1}{2},k} &= \frac{u_{i+\frac{1}{2},jk} + u_{i-\frac{1}{2},jk} + u_{i+\frac{1}{2},j+1,k} + u_{i-\frac{1}{2},j+1,k}}{4h} \left(\bar{v}_{i+\frac{1}{2},j+\frac{1}{2},k} - \bar{v}_{i-\frac{1}{2},j+\frac{1}{2},k} \right) \\
&+ \frac{v_{i,j+\frac{1}{2},k}}{h} \left(\bar{v}_{i,j+1,k} - \bar{v}_{ijk} \right) \\
&+ \frac{w_{ij,k+\frac{1}{2}} + w_{ij,k-\frac{1}{2}} + w_{i,j+1,k+\frac{1}{2}} + w_{i,j+1,k-\frac{1}{2}}}{4h} \left(\bar{v}_{i,j+\frac{1}{2},k+\frac{1}{2}} - \bar{v}_{i,j+\frac{1}{2},k-\frac{1}{2}} \right).
\end{aligned}
$$

The algorithm for calculating $\bar{v}_{i,j+1,k}$ is given as

$$
\bar{v}_{i,j+1,k} = v_{ilk} + \frac{h}{2}\gamma_v(1 - 2(l - (j + \frac{1}{2}))),
$$

$$
l = \begin{cases} j + \frac{1}{2} & \text{if } v_{i,j+1,k} > 0, \\ j + \frac{3}{2} & \text{otherwise,} \end{cases}
$$

$$
\alpha_v = \frac{v_{ilk} - v_{i,l-1,k}}{h}, \quad \beta_v = \frac{v_{i,l+1,k} - v_{ilk}}{h}, \quad \gamma_v = \begin{cases} \alpha_v & \text{if } |\alpha_v| \leq |\beta_v|, \\ \beta_v & \text{otherwise,} \end{cases}
$$

where $v_{i,j+1,k} = 0.5(v_{i,j+\frac{3}{2},k} + v_{i,j+\frac{1}{2},k})$. The other quantities are similarly computed. We then discretize the advection term in Eq. (16) as follows:

$$
\begin{aligned}
(\mathbf{u} \cdot \nabla_h w)_{ij,k+\frac{1}{2}} &= \frac{u_{i+\frac{1}{2},jk} + u_{i-\frac{1}{2},jk} + u_{i+\frac{1}{2},j,k+1} + u_{i-\frac{1}{2},j,k+1}}{4h} \left(\bar{w}_{i+\frac{1}{2},j,k+\frac{1}{2}} - \bar{w}_{i-\frac{1}{2},j,k+\frac{1}{2}} \right) \\
&+ \frac{v_{i,j+\frac{1}{2},k} + v_{i,j-\frac{1}{2},k} + v_{i,j+\frac{1}{2},k+1} + v_{i,j-\frac{1}{2},k+1}}{4h} \left(\bar{w}_{i,j+\frac{1}{2},k+\frac{1}{2}} - \bar{w}_{i,j-\frac{1}{2},k+\frac{1}{2}} \right) \\
&+ \frac{w_{ij,k+\frac{1}{2}}}{h} \left(\bar{w}_{ij,k+1} - \bar{w}_{ijk} \right).
\end{aligned}
$$

The algorithm for calculating $\bar{w}_{ij,k+1}$ is given as

$$
\bar{w}_{ij,k+1} = w_{ijl} + \frac{h}{2}\gamma_w(1 - 2(l - (k + \frac{1}{2}))),
$$

$$
l = \begin{cases} k + \frac{1}{2} & \text{if } w_{ij,k+1} > 0, \\ k + \frac{3}{2} & \text{otherwise,} \end{cases}
$$

$$
\alpha_w = \frac{w_{ijl} - w_{ij,l-1}}{h}, \quad \beta_w = \frac{w_{ij,l+1} - w_{ijl}}{h}, \quad \gamma_w = \begin{cases} \alpha_w & \text{if } |\alpha_w| \leq |\beta_w|, \\ \beta_w & \text{otherwise,} \end{cases}
$$

where $w_{ij,k+1} = 0.5(w_{ij,k+\frac{3}{2}} + w_{ij,k+\frac{1}{2}})$. The other quantities are similarly computed.

References

[1] A.J. Chorin, A numerical method for solving incompressible viscous flow problems, J. Comput. Phys. 2 (1967) 12–26.

[2] M.-J. Ni, M.A. Abdou, A bridge between projection methods and SIMPLE type methods for incompressible Navier–Stokes equations, Internat. J. Numer. Methods Engrg. 72 (2007) 1490–1512.

[3] J. Shen, On error estimates of projection methods for Navier–Stokes equations: first-order schemes, SIAM J. Numer. Anal. 29 (1) (1992) 57–77.

[4] J. Shen, X. Yang, Decoupled, energy stable schemes for phase-field models of two-phase incompressible flows, SIAM J. Numer. Anal. 53 (1) (2015) 279–296.

[5] Y. Di, R. Li, T. Tang, P. Zhang, Moving mesh finite element methods for the incompressible Navier–Stokes equations, SIAM J. Sci. Comput. 26 (3) (2005) 1036–1056.

[6] F. Zhang, J. Cheng, T. Liu, A direct discontinuous Galerkin method for the incompressible Navier–Stokes equations on arbitrary grids, J. Comput. Phys. 380 (2019) 269–294.

[7] L. Lin, Z. Yang, S. Dong, Numerical approximation of incompressible Navier–Stokes equations based on an auxiliary energy variable, J. Comput. Phys. 388 (2019) 1–22.

[8] P. Suchde, J. Kuhnert, S. Tiwari, On meshfree GFDM solvers for the incompressible Navier–Stokes equations, Comput. & Fluids 165 (30) (2018) 1–12.

[9] E. Castillo, R. Codina, Dynamic term-by-term stabilized finite element formulation using orthogonal subgrid-scales for the incompressible Navier–Stokes problem, Comput. Methods Appl. Mech. Engrg. 349 (1) (2019) 701–721.

[10] F. Qu, D. Sun, J. Bai, A new genuinely two-dimensional Reimann solver for multidimensional Euler and Navier–Stokes equations, Comput. Phys. Comm. 243 (2019) 1–11.

[11] J. Deteix, D. Yakoubi, Shear rate projection schemes for non-Newtonian fluids, Comput. Methods Appl. Mech. Engrg. 354 (1) (2019) 620–636.

[12] H.C. Elman, T. Su, A low-rank solver for the stochastic unsteady Navier–Stokes problem, Comput. Methods Appl. Mech. Engrg. 364 (1) (2020) 112948.

[13] Z. Guo, P. Lin, J. Lowengrub, S.M. Wise, Mass conservative and energy stable finite difference methods for the quasi-incompressible Navier–Stokes–Cahn–Hilliard system: Primitive variable and projection-type schemes, Comput. Methods Appl. Mech. Engrg. 326 (1) (2017) 144–174.

[14] J. Yang, S. Mao, X. He, X. Yang, Y. He, A diffuse interface model and semi-implicit energy stable finite element method for two-phase magnetohydrodynamic flows, Comput. Methods Appl. Mech. Engrg. 356 (1) (2019) 435–464.

[15] H.G. Lee, K. Kim, J. Kim, On the long time simulation of the Rayleigh–Taylor instability, Internat. J. Numer. Methods Engrg. 85 (2011) 1633–1647.

[16] H. Ding, P.D.M. Spelt, C. Shu, Diffuse interface model for incompressible two-phase flows with large density ratios, J. Comput. Phys. 226 (2) (2007) 2078–2095.

[17] C.-Y. Zhang, H. Ding, P. Gao, Y.-L. Wu, Y-l wu diffuse interface simulation of ternary fluids in contact with solid, J. Comput. Phys. 309 (2016) 37–51.

[18] R.H. Nochetto, A.J. Salgado, I. Tomas, A diffuse interface model for two-phase ferrofluid flows, Comput. Methods Appl. Mech. Engrg. 309 (2016) 497–531.

[19] P.-H. Chiu, A coupled phase field framework for solving incompressible two-phase flows, J. Comput. Phys. 392 (2019) 115–140.

[20] C. Liu, F. Frank, C. Thiele, F.O. Alpak, S. Berg, W. Chapman, B. Riviere, An efficient numerical algorithm for solving viscosity contrast Cahn–Hilliard–Navier–Stokes system in porous media, J. Comput. Phys. 400 (2020) 108948.

[21] G. Zhu, H. Chen, J. Yao, S. Sun, Efficient energy-stable schemes for the hydrodynamics coupled phase-field model, Appl. Math. Model 70 (2019) 82–108.

[22] G. Zhu, H. Chen, A. Li, S. Sun, J. Yao, Fully discrete energy stable scheme for a phase-field moving contact line model with variable densities and viscosities, Appl. Math. Model 83 (2020) 614–639.

[23] J. Zhang, C. Chen, J. Wang, X. Yang, Efficient, second order accurate and unconditionally energy stable numerical scheme for a new hydrodynamics coupled binary phase-field surfactant system, Comput. Phys. Comm. 251 (2020) 107122.

[24] Q. Zhang, X.-P. Wang, Phase field modeling and simulation of three-phase flow on solid surfaces, J. Comput. Phys. 319 (2016) 79–107.

[25] Q. Du, L. Ju, L. Tian, Finite element approximation of the Cahn–Hilliard equation on surfaces, Comput. Methods Appl. Mech. Engrg. 200 (29–32) (2011) 2458–2470.

[26] Y. Li, J. Kim, N. Wang, An unconditionally energy-stable second-order time-accurte scheme for the Cahn–Hilliard equation on surfaces, Commun. Nonlinear Sci. Numer. Simul. 53 (2017) 213–227.

[27] G. Dziuk, C.M. Elliott, Surface finite elements for parabolic equations, J. Comput. Math. 25 (4) (2007) 385–407.

[28] J.B. Green, A.L. Bertozzi, G. Sapiro, Fourth order paratial differential equations on general geometries, J. Comput. Phys. 216 (1) (2006) 216–246.

[29] S. Zhao, X. Xiao, X. Feng, An efficient time adaptivity based on chemical potential for surface Cahn–Hilliard equation using finite element approximation, Appl. Math. Comput. 369 (2020) 124901.

[30] Y. Choi, D. Jeong, S. Lee, M. Yoo, J. Kim, Motion by mean curvature of curves on surfaces using the Allen–Cahn equation, Internat. J. Engrg. Sci. 97 (2015) 126–132.

[31] X. Xiao, R. He, X. Feng, Unconditionally maximum principle preserving finite element schemes for the surface Allen–Cahn type equations, Numer. Methods Partial Differential Equations (2019) http://dx.doi.org/10.1002/num.22435.

[32] H.G. Lee, J. Kim, A simple and efficient finite difference method for the phase-field crystal equation on curved surfaces, Comput. Methods Appl. Mech. Engrg. 307 (2016) 32–43.

[33] Y. Li, C. Luo, B. Xia, J. Kim, An efficient linear second order unconditionally stable direct discretization method for the phase-field crystal equation on surfaces, Appl. Math. Model 67 (2019) 477–490.

[34] D. Jeong, J. Kim, Microphase separation patterns in diblock copolymers on curved surfaces using a nonlocal Cahn–Hilliard equation, Eur. Phys. J. E 38 (2015) 117.

[35] M.S. Mohamed, A.N. Hirani, R. Samtaney, Discrete exterior calculus discretization of incompressible Navier–Stokes equations over surface simplicial meshes, J. Comput. Phys. 312 (1) (2016) 175–191.

[36] I. Nitschke, S. Reuther, A. Voigt, Discrete exterior calculus (DEC) for the surface Navier–Stokes equation, 2017, http://dx.doi.org/10.1007/978-3-319-56602-3_7.

[37] S. Reuther, A. Voigt, Solving the incompressible surface Navier–Stokes equation by surface finite elements, Phys. Fluids 30 (2018) 012107.

[38] J. Yang, Y. Li, J. Kim, A practical finite difference scheme for the Navier–Stokes equation on curved surfaces in $\mathbb{R}^3$, J. Comput. Phys. 411 (2020) 109403.

[39] V.E. Ambrus, S. Busuioc, A.J. Wagner, F. Paillusson, H. Kusumaatmaja, Multicomponent flow on curved surfaces: A vielbein lattice Boltzmann approach, Phys. Rev. E 100 (2019) 063306.

[40] I. Nitschke, A. Voigt, J. Wensch, A finite element approach for incompressible two-phase flow on manifolds, J. Fluid Mech. 708 (2012) 418–438.

[41] F.H. Harlow, J.E. Welch, Numerical calculation of time-dependent viscous incompressible flow of fluid with free surface, Phys. Fluids 8 (12) (1965) 2182–2189.

[42] D.J. Eyre, Unconditionally gradient stable time marching the Cahn–Hilliard equation, in: J.W. Bullard, L.Q. Chen (Eds.), MRS Proceedings, in: Computational and mathematical models of microstructural evolution, vol. 529, Cambridge University Press, 1998, pp. 39–46.

[43] J.B. Greer, An improvement of a recent Eulerian method for solving PDEs on general geometries, J. Sci. Comput. 29 (2006) 321–352.

[44] D. Jeong, Y. Li, Y. Choi, M. Yoo, D. Kang, J. Park, J. Choi, J. Kim, Numerical simulation of the zebra pattern formation on a three-dimensional model, Physica A 475 (2017) 106–116.

[45] G. Zhu, J. Kou, B. Yao, Y-s. Wu, J. Yao, S. Sun, Thermodynamically consistent modelling of two-phase flows with moving contact line and soluble surfactants, J. Fluid Mech. 879 (2019) 327–359.

[46] S.J. Ruuth, B. Merriman, A simple embedding method for solving partial differential equations on surfaces, J. Comput. Phys. 227 (2008) 1943–1961.

[47] C.B. Macdonald, J. Brandman, S.J. Ruuth, Solving eigenvalue problems on curved surfaces using the closest point method, J. Comput. Phys. 230 (2011) 7944–7956.

[48] Y. Li, A. Yun, D. Lee, J. Shin, D. Jeong, J. Kim, Three-dimensional volume-conserving immersed boundary model for two-phase fluid flows, Comput. Methods Appl. Mech. Engrg. 257 (2013) 36–46.

[49] S. Lee, D. Jeong, W. Lee, J. Kim, An immersed boundary method for a contractile elastic ring in a three-dimensional Newtonian fluid, J. Sci. Comput. 67 (2016) 909–925.

[50] X. Pan, K. Kim, C. Lee, J.-I. Choi, A decoupled monolithic projection method for natural convection problems, J. Comput. Phys. 314 (2016) 160–166.

[51] X. Pan, K. Kim, C. Lee, J.-I. Choi, Fully decoupled monolithic projection method for natural convection problems, J. Comput. Phys. 334 (2017) 582–606.

[52] C.W. Shu, S. Osher, Efficient implementation of essentially non-oscillatory shock capturing schemes II, J. Comput. Phys. 83 (1989) 32–78.

[53] J. Kim, An augmented projection method for the incompressible Navier–Stokes equations in arbitrary domains, Int. J. Comput. Methods 2 (2) (2005) 201–212.

[54] H.G. Lee, J. Kim, Numerical simulation of the three-dimensional Rayleigh–Taylor instability, Comput. Math. Appl. 66 (2013) 1466–1474.

[55] D. Jeong, Y. Li, C. Lee, J. Yang, J. Kim, A conservative numerical method for the Cahn–Hilliard equation with generalized mobilities on curved surfaces in three-dimensional space, Commun. Comput. Phys. 27 (2020) 412–430.

[56] S. Wise, Unconditionally stable finite difference, nonlinear multigrid simulation of the Cahn–Hilliard–Hele–Shaw system of equations, J. Sci. Comput. 44 (2010) 38–68.

[57] H.G. Lee, J. Kim, Two-dimensional Kelvin–Helmholtz instabilities of multi-component fluids, Eur. J. Mech. B Fluids 49 (2015) 77–88.